

Topological phases in iridium oxide superlattices: Quantized anomalous charge or valley Hall insulators

Yige Chen¹ and Hae-Young Kee^{1,2,*}¹*Department of Physics, University of Toronto, Ontario, Canada M5S 1A7*²*Canadian Institute for Advanced Research, CIFAR Program in Quantum Materials, Toronto, Ontario, Canada M5G 1Z8*

(Received 23 June 2014; revised manuscript received 4 October 2014; published 24 November 2014)

We study topological phases in orthorhombic perovskite iridium (Ir) oxide superlattices grown along the [001] crystallographic axis. Bilayer Ir oxide superlattices display topological magnetic insulators exhibiting quantized anomalous Hall effects due to strong spin-orbit coupling of Ir $5d$ orbitals and electronic correlation effects. We also find a valley Hall insulator with counterpropagating edge currents from two different valleys and a topological crystalline insulator with edge states protected by the crystal lattice symmetry based on stacking of two layers. In a single-layer superlattice, a topological insulator can be realized, when a strain field is applied to break the symmetry of a glide plane protecting the Dirac points. It turns into a topological magnetic insulator in the presence of magnetic ordering and/or in-plane magnetic field. We discuss essential ingredients for these topological phases and experimental signatures to test our theoretical proposals.

DOI: [10.1103/PhysRevB.90.195145](https://doi.org/10.1103/PhysRevB.90.195145)

PACS number(s): 71.20.Be, 71.30.+h, 72.15.-v, 73.43.Cd

I. INTRODUCTION

Considerable attention has recently been devoted to the study of nontrivial physics arising from strong spin-orbit coupling (SOC). Such studies were initiated by theoretical proposals of topological insulators with conducting surface states protected by time-reversal (TR) symmetry [1–9], which was then experimentally confirmed in two-dimensional (2D) HgTe/Hg_{1-x}Cd_xTe quantum wells [10] and indirectly by angle-resolved photoemission spectroscopy (ARPES) in three-dimensional (3D) systems such as Bi_{1-x}Sb_x [11,12], Bi₂Se₃ [13,14], Bi₂Te₃, and Sb₂Te₃ [15–17]. Since then, a variety of topological phases has been theoretically suggested. These include topological crystalline insulators with surface states protected by crystal lattice symmetry [18–22], Weyl semimetals with chiral fermions [23–27], and topological magnetic insulators with quantized anomalous Hall (QAH) effects [28–31]. Furthermore, strongly interacting systems could provide a new avenue to explore more exotic phases such as topological Mott insulators and fractional Chern insulators [32,33].

While the number of topological phases proposed in theory is still growing, experimental confirmations are limited to the systems of groups IV–VI elements. Why have such topological phases not been detected in other abundant materials such as oxides? In particular, transition-metal oxides exhibit various collective phenomena stemming from strong electronic correlations, and this has led to tremendous interest and effort in growing oxide films to discover new functionalities. However, this effort has so far been focused mainly on $3d$ - and $4d$ -orbital systems with weak or moderate SOC, and little attention has been paid to $5d$ -orbital systems with strong SOC until recently.

Among $5d$ -orbital systems, Ir oxides named iridates have provided an excellent playground to study the combined effects of SOC and electron correlations. Depending on the underlying lattice structure, iridates have offered a rich phase diagram [33]. Despite different phases, a common ingredient is the

$J_{\text{eff}} = \frac{1}{2}$ description due to strong atomic SOC and this is a good starting point in building microscopic Hamiltonians. Using a $J_{\text{eff}} = \frac{1}{2}$ wave function, a topological insulator was proposed in 3D perovskite iridates [34]. It was found that bulk SrIrO₃ with $Pbnm$ structure exhibits a crystal-symmetry-protected nodal line which becomes a 3D nodal point when the mirror symmetry along the c axis is broken. It becomes a topological insulator with a large mirror symmetry-breaking term [34]. A successful growing of the Ir oxide superlattice [(SrIrO₃) _{n} ,SrTiO₃] where the integer n controls the number of Ir oxide layers using the pulsed laser deposition (PLD) technique has also been reported [35]. It has demonstrated how a spin-orbit magnetic insulator arises by tuning the number of SrIrO₃ layers.

Given that SrIrO₃ with $Pbnm$ structure possesses a crystal-symmetry-protected nodal line, it is possible to design other topological phases by employing the current experimental techniques. While a topological insulator was proposed in an effective honeycomb bilayer by fabricating a [111] superlattice structure from perovskite oxides [36], an atomically controlled [111] superlattice of perovskite oxides is known to be difficult to fabricate. On the other hand, an Ir oxide superlattice along the [001] axis has been successfully made by Matsuno *et al.* [35], as stated above. In this paper, we show how to realize topological phases in Ir oxide superlattices grown along the [001] axis, [(SrIrO₃) _{n} , (AMO₃) _{n'}], for integer n' and $n = 1$ or 2 , where AMO₃ is a band insulator with a closed-shell transition metal M^{4+} and an alkaline-earth metal A^{2+} . To realize topological phases, one has to retain oxygen octahedra rotation *and* tilting which is necessary to generate a Rashba-like SOC in the $J_{\text{eff}} = \frac{1}{2}$ basis. Thus, AMO₃ should have the orthorhombic $Pbnm$ structure such as CaTiO₃, SrZrO₃, or SrHfO₃ instead of SrTiO₃ with tetragonal structure. The topological states realized in these superlattices include topological magnetic insulators with QAH effects, nontrivial valley insulators, topological insulators with TR symmetry, and topological crystalline insulators.

This paper is organized as follows. In Sec. II, we show how a 2D topological insulator can be made in an Ir oxide

*hykee@physics.utoronto.ca

single-layer system. When oxygen octahedron is rotated and tilted away from the c axis, there are two 2D Dirac points similar to the honeycomb lattice [37]. These 2D Dirac points are protected by the b -glide symmetry. Breaking this b -glide symmetry generates a 2D topological insulator, and furthermore in the presence of a magnetic ordering and/or in-plane magnetic field, the system becomes a topological magnetic insulator. This could be confirmed by quantized Hall conductance in Hall measurement. In Sec. III, we propose two different types of bilayer Ir oxides. Depending on the layer stacking, one becomes a topological magnetic insulator for any small magnetic field that breaks the b -glide symmetry. The other case possesses various topological phases including topological crystalline, topological magnetic, and mirror valley insulators. In each section, we offer a schematic crystal structure of Ir oxide superlattices and physical origins of such topological phases based on symmetry of the lattice and TR. We summarize our findings in the last section.

II. SINGLE-LAYER IRIDATES

A. Model Hamiltonian and Dirac fermion

In bulk samples of AMO_3 with $Pbnm$ structure, each M atom surrounded by six O atoms forms an octahedron. This octahedron is rotated by an angle θ around the c axis and tilted by an angle ϕ around the local (110) direction, as shown in Fig. 1. The rotation and tilting angles alternate between two neighboring IrO_6 octahedra in the plane and between adjacent layers making four M atoms in a unit cell. To engineer a single-layer Ir oxide, the IrO_2 layer is grown from AMO_3 , as shown in Fig. 1. The x and y directions

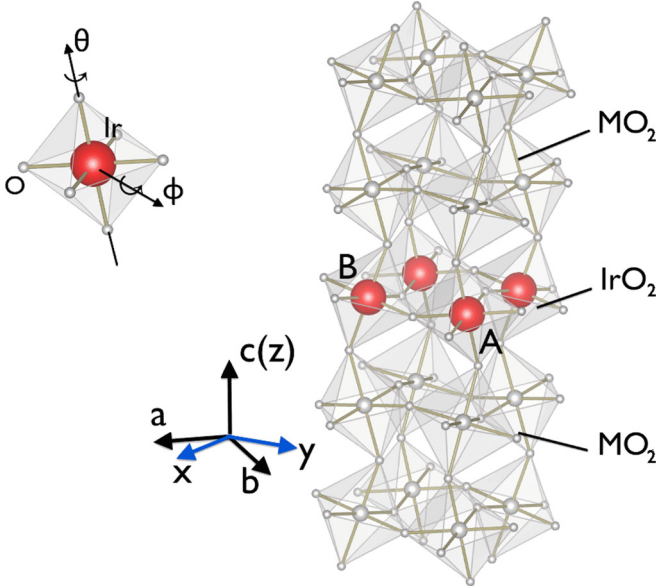


FIG. 1. (Color online) Left: IrO_6 octahedron with the rotation θ along the c axis and tilting ϕ along the local (110) axis. Right: Single-layer Ir oxide superlattice structure. IrO_2 layer contains two different sites denoted by A and B representing different rotations and tiltings, (θ, ϕ) and $(-\theta, -\phi)$ oxygen octahedra, and it is grown on a band insulator AMO_3 with $Pbnm$ structure. The primitive lattice vectors are $\vec{a} = (\hat{x} - \hat{y})/2$ and $\vec{b} = (\hat{x} + \hat{y})/2$.

are rotated by 45 degrees from the crystal a and b axis for convenience. As we state above, the alternating rotation and tilting of neighboring IrO_6 is crucial to realize topological phases for the following reason. The relatively strong SOC of Ir atoms splits t_{2g} states into $J_{\text{eff}} = \frac{1}{2}$ and $J_{\text{eff}} = \frac{3}{2}$, and the Ir^{4+} ionic configuration leading to the valence of $5d^5$ causes these iridates to be a half-filled $J_{\text{eff}} = \frac{1}{2}$ band. Even though the tetragonal distortion of IrO_6 octahedra may affect the validity of the $J_{\text{eff}} = \frac{1}{2}$ description in reality, the tetragonal crystal-field splitting is small compared to the SOC of iridium [38,39]. Thus, $J_{\text{eff}} = \frac{1}{2}$ states are well separated from $J_{\text{eff}} = \frac{3}{2}$ states, which makes the $J_{\text{eff}} = \frac{1}{2}$ picture still adequate to describe the physics near the Fermi energy. Note that $J_{\text{eff}} = \frac{1}{2}$ consists of $|J_z = \pm \frac{1}{2}\rangle = \frac{1}{\sqrt{3}}(|d_{xy,s} \pm |d_{yz,-s}\rangle + i|d_{xz,-s}\rangle)$, where $\pm s$ represents spin-1/2 up and down states [40], respectively. In the presence of the alternating tilting and rotation between neighboring sites, a hopping integral between $d_{xy,s}$ and $d_{xz/yz,s}$ orbitals becomes finite. Since $d_{xy,s}$ and $d_{xz/yz,s}$ belong to different spin states of $|J_z\rangle$, this hopping involves $|J_z = \frac{1}{2}\rangle$ and $|J_z = -\frac{1}{2}\rangle$ states, which then generates a spin-flip Rashba-like term.

For a single layer of IrO_2 , there are two sites due to different rotation (θ) and tilting angle (ϕ) between nearest-neighbor sites. We denote these Ir sites by A and B, indicating different oxygen environments as shown in Fig. 1. They have a rectangle structure associated with a glide symmetry plane, which corresponds to the invariance under a 1/2 translation along a certain direction, and reflection afterwards. In this lattice, it is along the b axis and thus named the b glide. The effect of this glide plane on t_{2g} orbitals is to interchange the d_{yz} with the d_{xz} orbital, and to exchange the A with the B site. Introducing the Pauli matrices $\vec{\tau}$ and $\vec{\sigma}$ for the sublattice A and B, and $J_{\text{eff}} = 1/2$ pseudospin, respectively, this b -glide symmetry plane is expressed as

$$\hat{\Pi}_b = \frac{i}{\sqrt{2}}(\sigma_x - \sigma_y)\tau_x \hat{k}_{bg}, \quad (1)$$

where \hat{k}_{bg} is the operator acting on crystal momentum space as $\hat{k}_{bg} : (k_x, k_y) \rightarrow (k_y, k_x)$ [34].

A tight-binding model can be constructed from $J_{\text{eff}} = 1/2$ bands with the basis $(A \uparrow, B \uparrow, A \downarrow, B \downarrow)$, where A and B denote two different Ir sites in the unit cell, as discussed above, and (\uparrow, \downarrow) represents $J_z = \pm \frac{1}{2}$. Taking into account nearest and next-nearest hoppings, the Hamiltonian is given by

$$H_0(\mathbf{k}) = \epsilon_0(\mathbf{k})\tau_x + \epsilon'(\mathbf{k})\mathbf{I} + \epsilon_{1d}(\mathbf{k})\sigma_z\tau_y + \epsilon_y(\mathbf{k})\sigma_y\tau_y + \epsilon_x(\mathbf{k})\sigma_x\tau_y, \quad (2)$$

where

$$\begin{aligned} \epsilon_{0/1d}(\mathbf{k}) &= 2t_{0/1d}[\cos(k_x) + \cos(k_y)], \\ \epsilon_{y/x}(\mathbf{k}) &= t_1 \cos(k_{x/y}) + t_2 \cos(k_{y/x}), \\ \epsilon'(\mathbf{k}) &= t' \cos(k_x) \cos(k_y). \end{aligned} \quad (3)$$

Here, t_0 is the nearest-neighbor (NN) intraorbital hopping and t_{1d} is the NN hopping between d_{yz} and d_{xz} orbitals. t' is the next-nearest-neighbor (NNN) intraorbital hopping. t_1 and t_2 are the NN hopping from d_{yz} and d_{xz} orbitals to d_{xy} orbital, respectively. t_{1d} , t_1 , and t_2 vanish without the

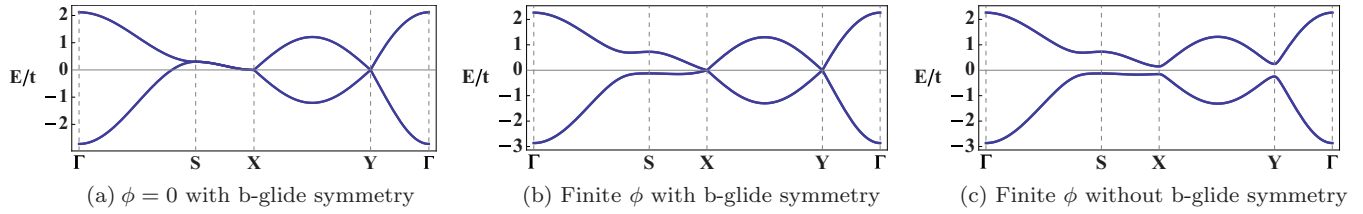


FIG. 2. (Color online) Band dispersion of single-layer Ir oxide (a) without tilting ϕ . It shows fourfold degeneracy along the $S = (\pi, 0) \rightarrow X = (\frac{\pi}{2}, -\frac{\pi}{2})$ direction. (b) Finite rotation and tilting leaves two Dirac points at X and $Y = (\frac{\pi}{2}, \frac{\pi}{2})$. (c) When the b -glide symmetry is broken, the Dirac point acquires a finite gap at the X and Y points. The set of (θ, ϕ) for both (b) and (c) is $(7^\circ, 19^\circ)$.

rotation and tilting of octahedra. The hopping parameters are obtained based on the Slater-Koster method [41] and the parameters are functions of θ and ϕ . For example, they are given by $(t', t_0, t_{1d}, t_1, t_2)/t = (-0.3, -0.6, -0.15, 0.15, 0.45)$ when $(\theta, \phi) \approx (7^\circ, 19^\circ)$, where t is the π bonding between d orbitals $t_{dd\pi}$, and we set $t_{dd\pi} : t_{dd\sigma} : t_{dd\delta} = 1 : \frac{3}{2} : \frac{1}{4}$. Note that the tight-binding parameters are fully determined by a set of (θ, ϕ) . Different values of (θ, ϕ) will simply modify the detailed shape of the band dispersion. Thus, by tuning the magnitude of (θ, ϕ) , it is possible to have the electron and hole pockets near Fermi energy. However, the topological feature of the band structure (characterized by the Chern numbers) remains intact. This particular choice of (θ, ϕ) is made to avoid the electron and hole pockets at ϵ_F , but topological properties do not depend on the choice of (θ, ϕ) .

The band structure is shown in Fig. 2. Without the tilting angle ϕ , two bands are degenerate along $X = (\frac{\pi}{2}, -\frac{\pi}{2})$ to $S = (\pi, 0)$, as shown in Fig. 2(a). However, when both rotation and tilting of octahedra are present, this degeneracy is broken, and there are two Dirac points at X and Y protected by the b -glide symmetry, as shown in Fig. 2(b). The Dirac point may appear below the Fermi energy ϵ_F when the tilting angle ϕ is not significant ($\phi < 17^\circ$). Indirect hopping via the oxygens can change the strength of hopping parameters as well, but the topological nature of phases described here is not altered by such quantitative changes. When the b -glide symmetry is broken, for example by a strain field along the x direction, these Dirac points are gapped, as shown in Fig. 2(c). In the following section, we discuss the topological nature of this insulator by providing the corresponding Chern numbers and edge state analysis.

B. Topological insulator and quantized anomalous Hall effects

Since the Dirac points are protected by the b -glide symmetry, any small perturbation that breaks the b -glide symmetry opens a gap at these two Dirac points. The b -glide operator is given by Eq. (1), and thus a small strain along the x (or y) direction is sufficient to break the b -glide symmetry. Such a broken b -glide symmetry term allows additional NNN and third-NN hoppings as follows:

$$\begin{aligned} \epsilon_{2n}(\mathbf{k}) &= [t_{2n} \cos(k_x + k_y) + t'_{2n} \cos(k_x - k_y)]\tau_z, \\ \epsilon_{3n}(\mathbf{k}) &= 2t_{3n}[\cos(2k_x) - \beta \cos(2k_y)]\tau_z, \end{aligned} \quad (4)$$

where t_{2n} and t_{3n} are the NNN intraorbital hopping, t_{3n} is the third-NN intraorbital hopping, and β is the parameter to measure the strength of a broken b -glide term. The tight-binding parameters $(t_{2n}, t'_{2n}, t_{3n}) = (0.098, -0.1, 0.06)$ obtained by Slater-Koster using the same set of angles (θ, ϕ) as above, and with $\beta = 0.6$ the band dispersion, are shown in Fig. 2(c).

The nontrivial topology behind the gapped Dirac point can be revealed through the following edge state calculation. The slab computation has been performed in a zigzag slab geometry periodic along $\vec{b} = \frac{\hat{x} + \hat{y}}{2}$, while it has an open boundary along $\vec{a} = \frac{\hat{x} - \hat{y}}{2}$. Along the \vec{a} direction, one end terminates at atom A and the other side ends with atom B . When TR symmetry is not broken, the system shows gapless edge modes propagating from the valence band to the conduction band, as shown in Fig. 3(a). These two gapless edge states cross at a time-reversal invariant momentum (TRIM) point, indicating their protection by the TR symmetry. As long as TR symmetry is present, the degeneracy cannot be lifted by disorders or weak interactions.

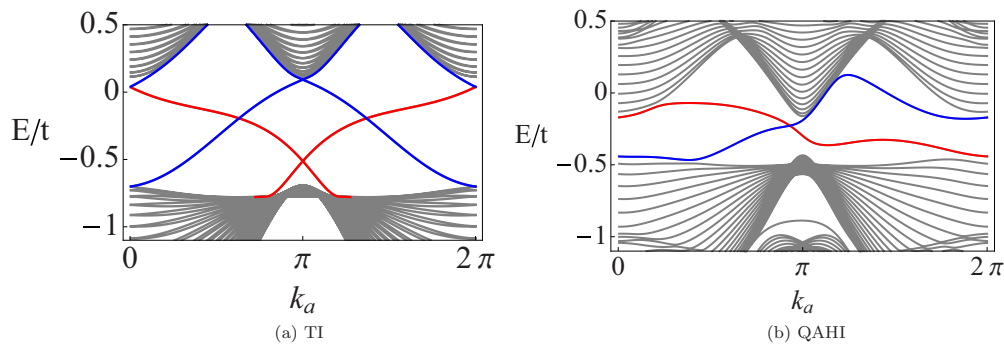


FIG. 3. (Color online) Edge state calculation of (a) the topological insulator (TI) shown in Fig. 2(c), and (b) the quantized anomalous Hall insulator (QAHI) when the TR is broken due to a noncollinear magnetic ordering or an in-plane magnetic field. Gray lines represent the bulk state and red (blue) lines denote the edge state at $L = 0$ ($L = N$) plotted along $k_a = k_x - k_y - \pi$. The parameter set is the same with the band dispersion in Fig. 2(c). The two gapless edge modes at $L = 0/L = N$ (red/blue) crossing at 1D TR invariant momentum indicate that the system belongs to a 2D TI. After breaking the TR, only one gapless edge state is left propagating along the boundary.

Indeed, we have checked that the edge states are robust, even in the presence of a random sublattice potential. The Z_2 index is another way to confirm the topological insulator. It is straightforward to compute the eigenvalues of the inversion operator [6]. The result shows that the Z_2 index = 1, consistent with the edge state calculation.

Another effect of strong SOC in iridates is an amplification of electronic correlation leading to a spin-orbit Mott insulator. The relevant bandwidth W is the $J_{\text{eff}} = \frac{1}{2}$ band rather than the full t_{2g} band due to the SOC, and thus the ratio of Hubbard interaction U and the bandwidth W is magnified in iridates [42,43]. In order to understand the magnetic ordering pattern, let us consider the Hubbard model with the tight-binding Hamiltonian of Eq. (2), where $\epsilon_{1d}(\mathbf{k})$ and $\epsilon_{y/x}(\mathbf{k})$ contain pseudospin-dependent terms. This NN Hamiltonian can be expressed as

$$H_0 = \sum_{\langle i,j \rangle} \{t_0 c_{i,A,\sigma}^\dagger c_{j,B,\sigma} + i c_{i,A,\alpha}^\dagger (\vec{v} \cdot \vec{\sigma})_{\alpha\beta} c_{j,B,\beta}\} + \text{H.c.},$$

where $\vec{v} = (\frac{t_x}{2}, \frac{t_y}{2}, t_{1d})$ along the x bond, while $\vec{v} = (\frac{t_x}{2}, \frac{t_y}{2}, t_{1d})$ along the y bond. Here $c_{i,A/B,\sigma}^\dagger$, in which the operator creates an electron on site i with sublattice A/B and pseudospin σ .

In the large- U limit, the spin model is then obtained as [44]

$$H_{\text{eff}} = J \sum_{\langle i,j \rangle} \vec{S}_i \cdot \vec{S}_j + \sum_{\langle i,j \rangle} \vec{D}_{ij} \cdot (\vec{S}_i \times \vec{S}_j). \quad (5)$$

Here, $J = \frac{4}{U} [(t_0)^2 - \vec{v} \cdot \vec{v}]$ and $\vec{D}_{ij} = \frac{8\epsilon_i t_0 \vec{v}}{U}$, where ϵ_i is the change of sign in the adjacent bond [33,45].

Note that when the bond retains the inversion symmetry, the Dzyaloshinskii-Moriya (DM) vector \vec{D} should vanish. However, due to the different rotation and tilting angles of oxygen octahedra between neighboring Ir atoms which break the inversion symmetry on the bond, the effective spin model of Eq. (5) is obtained. The ground state of such spin Hamiltonian has a noncollinear form,

$$m_{100}\sigma_x + m_{(010)}\sigma_y \tau_z + m_{(001)}\sigma_z \tau_z, \quad (6)$$

where $m_{(010)}$ and $m_{(001)}$ represent sublattice antiferromagnetic orderings, while $m_{(100)}$ denotes a ferromagnetic component of ordering. The exact form and amplitudes of the magnetic orderings in Eq. (6) are related to the crystal symmetry and detailed hopping parameters on the bond. However, the specific magnetic pattern is not crucial to realize the QAH effect in single-layer iridates, as long as the TR symmetry is broken.

In the absence of TR symmetry, the topological invariance characterizing the QAH effects is identified by the charge Chern number defined as

$$C_p = \frac{1}{2\pi} \int d^2\mathbf{k} \Omega_p^z(\mathbf{k}), \quad (7)$$

where p is the band index and $\Omega_p^z(\mathbf{k})$ is the z component of the p th-band Berry curvature $\Omega_p(\mathbf{k})$ given in the Appendix. The quantized transverse Hall conductance σ_{xy} is then given by

$$\sigma_{xy} = \frac{e^2}{h} \sum_{p \in \text{occupied}} C_p, \quad (8)$$

where the sum goes over all occupied bands below Fermi energy ϵ_F . For the single-layer 2D Ir oxide, the quantized Hall

conductivity is obtained as

$$\sigma_{xy} = \frac{e^2}{h}, \quad (9)$$

indicating the topological invariance $C \equiv \sum_{p \in \text{occupied}} C_p = 1$ related to the edge currents propagating along one direction on the sample boundary [46] shown in Fig. 3(b).

Note that the QAH phase depends on the magnitude of the ordering. The different sizes of gaps at the X and Y points appear after breaking b -glide symmetry; see Fig. 2(c). If the strength of the magnetic ordering reverses the bands at the X point, for instance, while keeping the gap at the Y point intact, the system turns into the QAH phase with quantized σ_{xy} of Eq. (9). However, if the magnitude of the ordering is sufficiently large to reverse both bands at the X and Y points, the system will then turn to a trivial insulator. Thus, above the magnetic ordering temperature, the QAH phase should show up in a certain range of external magnetic field.

III. BILAYER IRIDATES

To realize the topological phases in the single-layer IrO₂ layer, the b -glide symmetry should be externally broken. This requires a strain field in a certain direction, which is not trivial in an experimental setting. In this section, we propose two types of bilayer IrO₂ systems, which naturally hold topological phases without a lattice symmetry-breaking perturbation. Since the single IrO₂ layer has two different sets of rotation and tilting angles, one way to engineer bilayer systems is to stack two layers of A and B on top of each other. Note that A and B per unit cell have the rotation and tilting angle (θ, ϕ) and $(-\theta, -\phi)$, respectively. Another way to stack two single layers is to make the second layer have different rotation and tilting set such as $(\theta, -\phi)$ and $(-\theta, \phi)$ denoted by C and D sites, respectively. We call the first case $ABAB$ stacking and the other case $ABCD$ stacking; see Fig. 4. The distance between the top and bottom layers in both cases can be manipulated by the number of AMO₃ layers in between, and the nature of topological phases is not altered by such quantitative changes. Let us consider the $ABAB$ stacking case first.

A. $ABAB$ stacking

As presented in Fig. 4, the $ABAB$ bilayer structure with significant rotation and tilting can be obtained by inserting a single-layer band insulator material MO_2 ($M = \text{Zr, Hf}$) between two IrO₂ layers. The tight-binding Hamiltonian is given by

$$H_{ABAB}(\mathbf{k}) = \sum_{i=1,2} H_0^i(\mathbf{k}) + H_{12}(\mathbf{k}), \quad (10)$$

where H_0^i represents a top ($i=1$) and bottom ($i=2$) IrO₂ layer and is the same as Eq. (2). H_{12} contains the hopping terms between the two layers and, introducing another Pauli matrices \vec{v} for the layer degree of freedom, it is

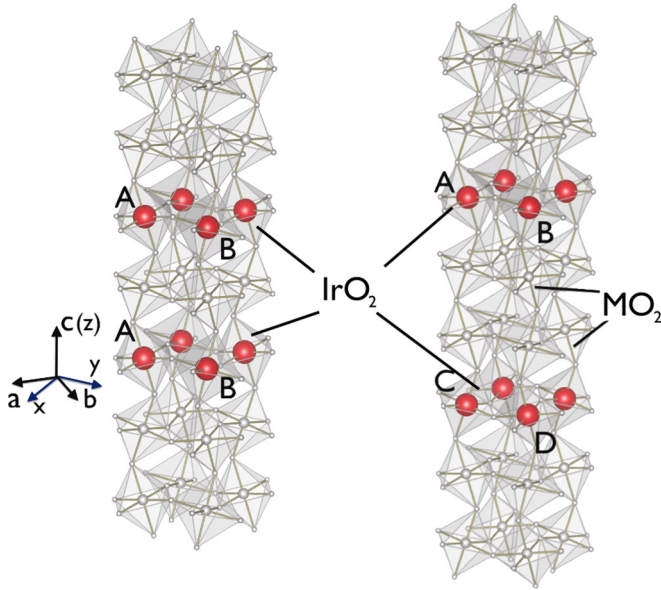


FIG. 4. (Color online) Left: *ABAB* stacking with $A = (\theta, \phi)$ and $B = (-\theta, -\phi)$ types of octahedra rotation and tilting. Right: *ABCD* bilayer stacking which contains A and B in the top layer, while $C = (\theta, -\phi)$ and $D = (-\theta, \phi)$ types of octahedra rotation and tilting are in the bottom layer.

written as

$$\begin{aligned}
 H_{12}(\mathbf{k}) = & \epsilon_{di}(\mathbf{k})v_x + \text{Re}[\epsilon_{dz}(\mathbf{k})]\sigma_y\tau_yv_x + \text{Im}[\epsilon_{dz}(\mathbf{k})]\sigma_z\tau_yv_y \\
 & + \text{Re}[\epsilon_z(\mathbf{k})]\sigma_y\tau_yv_x + \text{Im}[\epsilon_z(\mathbf{k})]\sigma_x\tau_yv_x \\
 & + \text{Re}[\epsilon'_z(\mathbf{k})]\sigma_y\tau_yv_y + \text{Im}[\epsilon'_z(\mathbf{k})]\sigma_x\tau_yv_y, \quad (11)
 \end{aligned}$$

where

$$\begin{aligned}
 \epsilon_{di}(\mathbf{k}) = & t_z + t_{(110)} \cos(k_x + k_y) + t_{(1\bar{1}0)} \cos(k_x - k_y), \\
 \epsilon_{dz}(\mathbf{k}) = & t_{dz}[\cos(k_x) + \cos(k_y)] + it'_{dz}[\sin(k_x) + \sin(k_y)], \\
 \epsilon_z(\mathbf{k}) = & [t_{2z} \cos(k_y) + t_{1z} \cos(k_x)] + i(k_x \leftrightarrow k_y), \\
 \epsilon'_z(\mathbf{k}) = & [t'_{2z} \sin(k_y) + t'_{1z} \sin(k_x)] + i(k_x \leftrightarrow k_y). \quad (12)
 \end{aligned}$$

Here, t_z is the NN hopping between two layers. $t_{(110)}$ and $t_{(1\bar{1}0)}$ are the third-NN intraorbital hopping along (110) and $(1\bar{1}0)$, respectively. t_{dz} and t'_{dz} arise from the d_{yz} orbital to the d_{xz} orbital NNN hopping due to the rotation and tilting angles. t_{2z}, t_{1z}, t'_{2z} , and t'_{1z} are given by the overlap hopping integral between the $d_{yz}(d_{xz})$ and d_{xy} orbital. The parameters in the tight-binding Hamiltonian given by Eq. (10) are obtained based on the Slater-Koster method [41] and $(t_z, t_{(110)}, t_{(1\bar{1}0)}, t_{dz}, t'_{dz}, t_{2z}, t_{1z}, t'_{2z}, t'_{1z})/t = (-0.13, -0.01, -0.09, -0.03, -0.01, 0.014, 0.01, 0.062, 0.01)$ for the same θ and ϕ used in the single layer. The band structure in Fig. 5(a) shows that there are two line nodes around X and Y when $\phi = 0$. However, a finite tilting ϕ lifts the band degeneracy, but keeps one pair of Dirac points along the high symmetry line $X \rightarrow S$, which is protected by the b -glide symmetry in Fig. 5(b).

Due to the electronic correlation and DM interaction, a noncollinear magnetic ordering is expected. One example of

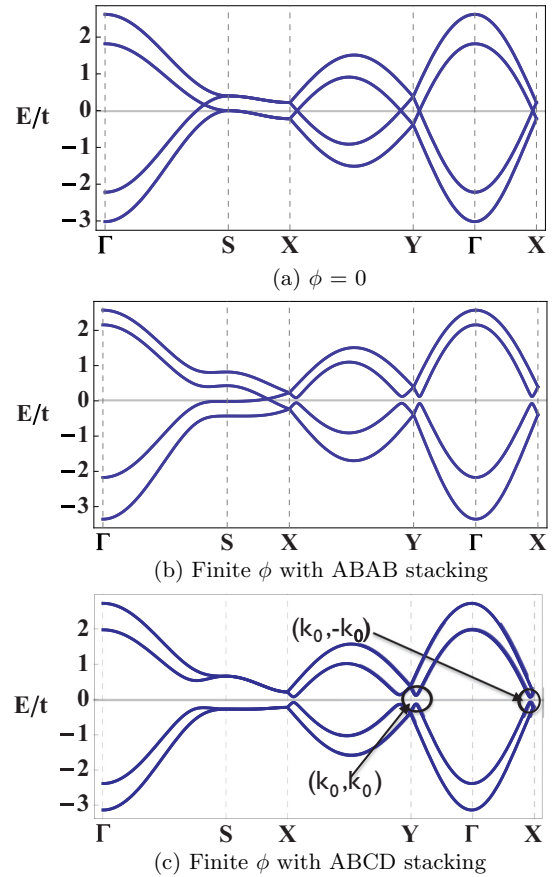


FIG. 5. (Color online) Band structure for bilayer with no tilt effect (i.e., $\phi = 0$) in octahedron environment (a) has a degenerate line circling the Γ point [47]. (b) *ABAB*: Finite tilting lifts the line node degeneracy but leaves one Dirac point protected by the b -glide symmetry along $S \rightarrow X$ for *ABAB* stacking. (c) Band structure for the *ABCD* bilayer with finite tilting ϕ . It has a band gap at $(k_0, \pm k_0)$ (circled out by band lines). The Fermi energy is $\epsilon_F = 0$, indicated by gray solid lines.

noncollinear orderings has the form

$$m_{(110)}(\sigma_x + \sigma_y) + m_{(1\bar{1}0)}(\sigma_x - \sigma_y)\tau_z + m_{(001)}\sigma_z\tau_z. \quad (13)$$

Since an exact direction of magnetic ordering is not important for the topological nature, we compute the Hall conductivity for (a) $m_{(110)} \neq 0$ and (b) $m_{(1\bar{1}0)} \neq 0$ cases. For both cases, we found it is quantized as

$$\sigma_{xy}^{\text{bilayer}} = 2 \frac{e^2}{h}, \quad (14)$$

which implies the charge Chern number defined in Eq. (7) for the entire valence bands $C = 2$. The edge states computed in the zigzag slab geometry are shown for the (a) case in Fig. 6(a) and the (b) case in Fig. 6(b), respectively. This also confirms the existence of the two gapless edge modes propagating along the sample boundary. Thus any magnetic ordering (or in-plane magnetic field) leads to a topological magnetic insulator with QAH effect in the 2D *ABAB* stacked bilayer Ir oxides.

The difference between the single-layer and the bilayer *ABAB* stacking deserves some discussion, as the bilayer is obtained simply by stacking the *AB* single layer. The Dirac

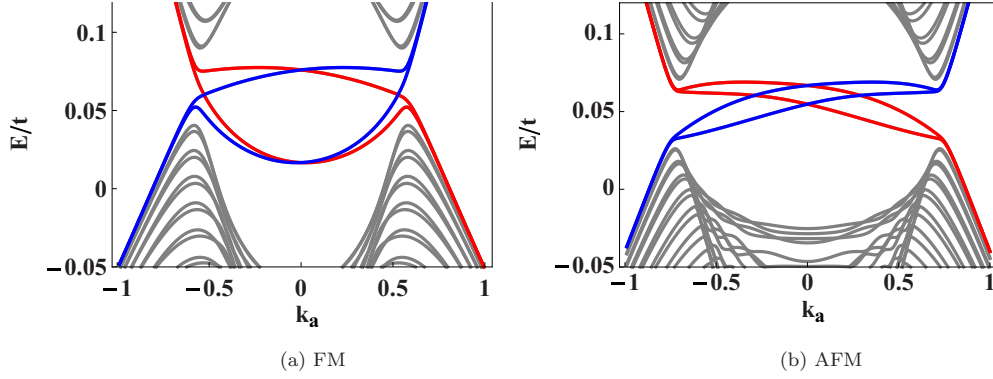


FIG. 6. (Color online) Slab dispersion with (a) ferromagnetic (FM) ordering with $m_{(110)} = 0.09t$ and (b) antiferromagnetic (AFM) ordering with strength $m_{(1\bar{1}0)} = 0.06t$. Two gapless edge modes at the $L = 0$ and $L = N$ boundaries are represented by red and blue, respectively.

nodes at the X and Y TRIM points of the single layer are protected by the b -glide symmetry. However, finite hopping integrals between two layers generate the different size of gaps at the X and Y points in the $ABAB$ bilayer system, and the Dirac point is shifted to a nonsymmetric point. Thus any magnetic field or magnetic ordering that breaks the b -glide symmetry would turn the system into a topological magnetic insulator. On the other hand, in the single layer, a magnetic field and/or ordering that breaks the TR and the b -glide symmetry simultaneously induces the same strength of gap at the X and Y points, making the system a trivial insulator. Thus an external b -glide symmetry-breaking perturbation is necessary to generate different gaps at X and Y in order to realize the QAH insulator in the single-layer case. Below we consider the other type of layer stacking, which offers various topological phases.

B. ABCD stacking

The crystal structure with $ABCD$ stacking is displayed in Fig. 4. The tight-binding Hamiltonian for this stacking is given by

$$H_{ABCD}(\mathbf{k}) = \sum_{i=\pm} H_0^i(\mathbf{k}) + H'_{12}(\mathbf{k}), \quad (15)$$

where

$$\begin{aligned} H_0^\pm(\mathbf{k}) &= \epsilon'(\mathbf{k})\mathbf{I} + \epsilon_0(\mathbf{k})\tau_x + \epsilon_{1d}(\mathbf{k})\sigma_z\tau_y \\ &\quad \pm[\epsilon_y(\mathbf{k})\sigma_y\tau_y + \epsilon_x(\mathbf{k})\sigma_x\tau_x], \\ H'_{12}(\mathbf{k}) &= \epsilon_{di}(\mathbf{k})v_x + \epsilon_{12}(\mathbf{k})\tau_x v_x + t'_z(\sigma_y + \sigma_x)\tau_z v_y. \end{aligned} \quad (16)$$

The various dispersions $\epsilon(\mathbf{k})$ s in H_0^\pm have the same expression as Eq. (3), which represent intralayer hopping integrals for the top ($i = +$) and bottom ($i = -$) layer. H'_{12} contains hopping paths between the two layers, and the dispersion $\epsilon_{di}(\mathbf{k})$ is the same as Eq. (12). t'_z represents the 1D orbital to d_{xy} -orbital hopping between the layers, and

$$\epsilon_{12}(\mathbf{k}) = t_{12}[\cos(k_x) + \cos(k_y)], \quad (17)$$

where t_{12} denotes the NNN interlayer intraorbital hopping.

In addition to the b -glide symmetry $\hat{\Pi}_b$ in Eq. (1), there exists another glide plane which transfers between top and

bottom layers in this bilayer system,

$$\hat{\Pi}_{\text{layer}} = \frac{i}{\sqrt{2}}(\sigma_x + \sigma_y)\tau_x v_x \hat{k}_{\text{layer}}, \quad (18)$$

where \hat{k}_{layer} is the operator that interchanges k_x with k_y as $\hat{k}_{\text{layer}} : (k_x, k_y) \rightarrow (-k_y, -k_x)$. By computing the commutator of $\hat{\Pi}_{\text{layer}}$ with $H_{ABCD}(\mathbf{k})$, it is straightforward to verify that $[\hat{\Pi}_{\text{layer}}, H_{ABCD}] = 0$.

The band dispersion is shown in Fig. 5(c). The set of tight-binding parameters is given by $(t_z, t_{(110)}, t_{1\bar{1}0}, t_{12}, t'_z)/t = (-0.23, -0.01, -0.09, -0.11, -0.04)$ for the same θ and ϕ in the single layer. The hopping amplitude changes as a function of distance and has been estimated by introducing a scaling function $1/r^5$. There are two line nodes that appear when the tilting degree vanishes, i.e., $\phi = 0$, and those degeneracies are gapped out after introducing some finite tilting, as shown in Fig. 5(c).

To analyze the topological nature of the bilayer system, we introduce the combined symmetry of $\hat{\Pi}_b$ and $\hat{\Pi}_{\text{layer}}$ such that $\hat{\Pi}_{\text{mirror}} \equiv \hat{\Pi}_b \hat{\Pi}_{\text{layer}} = i\sigma_z v_x \hat{k}$ with $\hat{k} : (k_x, k_y) \rightarrow (-k_x, -k_y)$, since the Hamiltonian is even under \hat{k} , $[i\sigma_z v_x, H_{ABCD}] = 0$. Furthermore, the low-energy effective Hamiltonian can be brought into a block diagonalized form near X and Y TRIM points with each block labeled by the eigenvalues of $\sigma_z v_x$, given by

$$H_{\pm, X/Y}^{\text{eff}} = \vec{A}_{\pm, X/Y}(\mathbf{k}) \cdot \vec{\sigma}, \quad (19)$$

where \pm subscripts are assigned to reflect the eigenvalues of the combined operator $\hat{\Pi}_{\text{mirror}}$. The explicit expression of vector $\vec{A}_{\pm, X/Y}(\mathbf{k})$ is presented in the Appendix. One way to glimpse the topological phases lying behind the gapped band structure is to evaluate the topological charges [48] defined by the mirror valley (MV) Chern number C_{mv} , valley Chern number C_v , and mirror Chern number C_m , in addition to the charge Chern number C at the X and Y TRIM points:

$$\begin{aligned} C_{mv} &= \frac{1}{2}(C_{+,X} - C_{-,X} + C_{-,Y} - C_{+,Y}), \\ C_m &= \frac{1}{2}(C_{+,Y} - C_{-,Y} - C_{-,X} + C_{+,X}), \\ C_v &= (C_{+,X} + C_{-,X} - C_{+,Y} - C_{-,Y}), \\ C &= (C_{+,X} + C_{-,X} + C_{+,Y} + C_{-,Y}). \end{aligned} \quad (20)$$

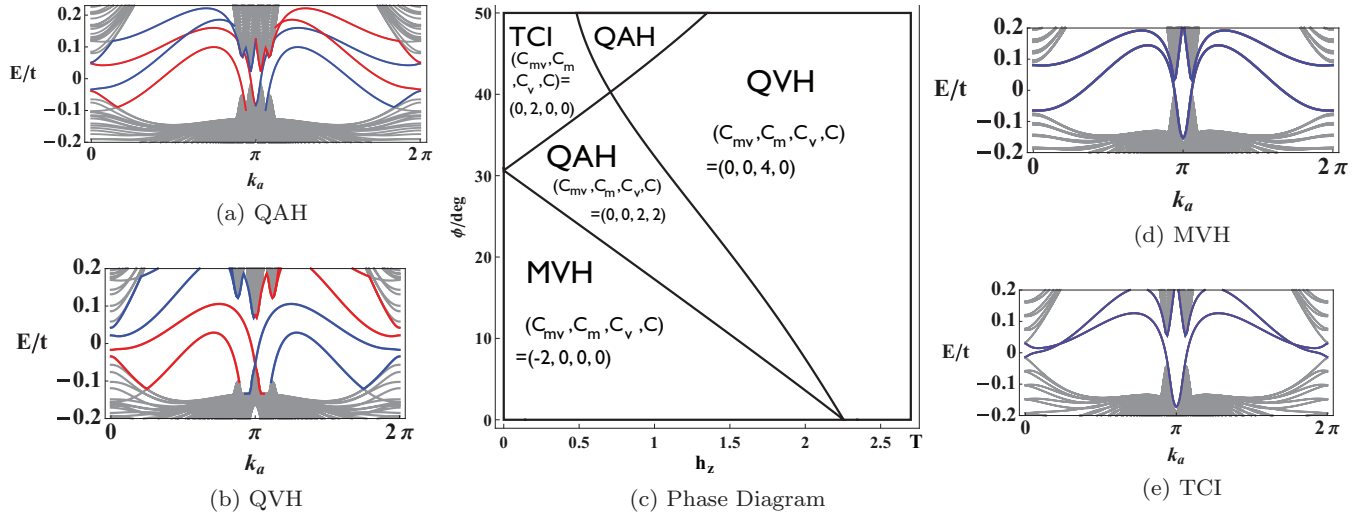


FIG. 7. (Color online) Phase diagram when rotation degree is $\theta = 13^\circ$ in (c) plotted as the z -direction exchange field h_z in units of Tesla (T) vs tilting degree ϕ . Different phases has been characterized by different topological invariants (C_{mv}, C_m, C_v, C) . The edge state for each phase has been displayed in (a) QAH, (b) quantized valley Hall (QVH), (d) mirror valley Hall (MVH), and (e) topological crystalline insulator (TCI). Two gapless edge modes in (a), (b), (d), and (e) at the $L = 0$ and $L = N$ boundaries are represented by red and blue, respectively. Edge states are purple (mixed color of red and blue) in (d) and (e) because of the degeneracy between edge modes at $L = 0$ and $L = N$. See the main text for finite C_{mv} and C_m related to these edge modes.

The charge Chern number C is the sum of all Chern numbers $C_{\pm, X/Y}$ associated with valleys (X/Y) and mirror symmetry eigenvalues (\pm). The valley-Chern/mirror-Chern number C_v/C_m is odd only under the interchange of two valley/mirror symmetry eigenvalues. The mirror valley Chern number C_{mv} , however, is odd under the interchange of valleys and mirror symmetry eigenvalues, respectively. The computation details of (C_{mv}, C_m, C_v, C) and the explicit expressions are presented in the Appendix.

A phase diagram contains various phases [49] including the mirror valley Hall phase, topological crystalline insulator phase, QAH phase, and quantized valley Hall phase with distinguished topological features, as displayed in Fig. 7(c). The phases listed here are robust against disorder as long as it preserves the symmetry associated with each phase [19,37,50]. The vertical axis is the degree of tilting angle ϕ and the horizontal axis corresponds to the strength of the z component of the magnetic exchange field and/or ordering. The phase boundaries can be modified depending on the magnetic ordering or exchange field pattern, but the qualitative picture of the phase diagram is not sensitive to the choice of magnetic ordering direction, as long as there is a finite z component of ferromagnetic h_z or antiferromagnetic ordering of m_z . Thus we only tune the strength of h_z for simplicity. In Fig. 7(c), h_z is estimated in Tesla using the tight-binding parameters discussed above, and we set $t \sim 100$ meV.

Each phase separated by a thick black line in Fig. 7(c) is characterized by the unique set of topological invariance (C_{mv}, C_m, C_v, C) defined in Eq. (20). The edge states shown in Figs. 7(a), 7(b), 7(d), and 7(e) are obtained with the slab geometry under the same boundary condition with the *ABAB* stacking case described in the last section.

The bilayer with small tilting angle is characterized by the mirror valley Hall phase with $C_{mv} = -2$. The valley physics in the mirror valley Hall phase manifests explicitly in the edge

state dispersion in Fig. 7(d). When the degree of tilting angle ϕ increases, it becomes a topological crystalline insulator with $C_m = 2$. The large tilting degree is able to inverse the sign of one of the mass terms near X or Y , and thus modifies the topology of the system. The edge state dispersion for the topological crystalline insulator phase in Fig. 7(e) has two pairs of gapless currents moving along opposite directions on each boundary. Each pair of edge modes carries opposite mirror eigenvalues. As the name suggests, these two pairs of gapless edge states are indeed protected by $\hat{\Pi}_{\text{mirror}}$. A TR breaking term will not lift the degeneracy between edge states as long as the perturbation preserves $\hat{\Pi}_{\text{mirror}}$.

By tuning the strength of h_z , the QAH phase arises. In the QAH phase, two gapless edge states localized at $L = 0$ propagate along the same direction. Each one contributes e^2/h to the Hall conductance and the total Hall conductivity, when Fermi energy has been tuned inside the bulk gap and is given by

$$\sigma_{xy} = 2 \frac{e^2}{h}. \quad (21)$$

However, in the quantized valley Hall phase, within valley X (Y), the two edge states localized at $L = 0$ propagating along the same direction lead to quantized valley Hall conductivity σ_{xy}^v ,

$$\sigma_{xy}^v = C_v \frac{e^2}{h} = 4 \frac{e^2}{h}. \quad (22)$$

In order to detect the anomalous Hall conductivity σ_{xy}^v , photon illumination with circularly polarized light can be used, which has been reported in the monolayer MoS_2 transistors [51]. Since these two valleys are related by the inversion symmetry, it requires breaking of the inversion symmetry to measure the valley Hall conductance in Eq. (22).

The mirror and mirror valley Chern numbers (C_m, C_{mv}) can be understood through the behavior of edge modes localized at $L = 0$, for instance. When the system is in the mirror valley Hall phase, there are four edge modes at $L = 0$ or $L = N$, as shown in Fig. 7(d). Two edge modes are propagating from left to right, labeled with $(-, X)$ and $(+, Y)$, respectively. The other two are flowing along the opposite direction, named as $(+, X)$ and $(-, Y)$, respectively. Here, $(\pm, X/Y)$ means the edge state carries \pm quantum number which is the eigenvalue of $\sigma_z \nu_x$ and the valley degree of freedom X/Y . Thus, C_{mv} is finite. When the gap is reversed at X , the propagating direction of the edge modes (\pm, X) will reverse and result in a nonvanishing C_m . Therefore, the system is a topological crystalline insulator, as shown in Fig. 7(e). ARPES has proven to be ideally suited to detect topological signatures of TCIs [22]; such methods can be, in principle, generalized to detect the MVH insulator.

As we emphasize above, a finite bilayer hopping integral is crucial to achieve the QAH phase when TR symmetry is broken because the z -axis ferromagnetic exchange field $h_z \sigma_z$ (or sublattice antiferromagnetic ordering $m_z \tau_z \sigma_z$) has to overcome t_z to reverse the sign of the Berry curvature around X or Y in order to enter the QAH insulator phase (see the Appendix for the proof). Using the current tight-binding parameters, the strength of h_z needs to be about a few Tesla, as shown in Fig. 7(c). Since the critical strength of h_z is tuned by the strength of t_z , it is desirable to make the bilayer hopping t_z smaller, which can be controlled by the spacing between the layers, as shown in Fig. 4.

IV. CONCLUSIONS

A recent experiment has reported the successful growth of an Ir oxide superlattice $[(\text{SrIrO}_3)_n, \text{SrTiO}_3]$, with a controllable number of layers n , which tailors a spin-orbit magnetic insulator for $n = 1$ and 2 [35]. Due to the smaller lattice constant in TiO_2 compared with IrO_2 , it was expected that there are alternating rotations of Ir octahedra, but lacking the tilting (ϕ) of octahedra to keep the tetragonal crystal structure of SrTiO_3 . This was confirmed by the magnetic ordering patterns in $n = 1$ and 2 superlattices, consistent with the first-principles calculations [35]. However, topological phases have not been observed in these superlattices, even though bulk SrIrO_3 orthorhombic perovskites possess a crystal-symmetry-protected nodal line [34].

One essential ingredient to realize any topological insulator is a Rashba-like SOC. In the $J_{\text{eff}} = 1/2$ wave function formed by a strong atomic SOC, this Rashba-like SOC is generated by finite hopping integrals between different $J_z = \pm 1/2$ states. For example, finite hopping paths between d_{xy} and $d_{xz/yz}$ generate Rashba-like SOC terms in the $J_{\text{eff}} = 1/2$ basis since d_{xy} up-spin and one-dimensional orbitals of $d_{xz/yz}$ up-spin belong to different J_z states. In layered perovskite systems, this is possible when the hopping path does not respect the mirror symmetry under $z \rightarrow -z$, as d_{xy} is even while $d_{xz/yz}$ is odd under this operation. Thus the alternating octahedra rotations and tiltings are necessary for topological phases in layered perovskites.

We propose topological phases in Ir oxide superlattices or films. Different topological phases were found depending on how the TR and crystal symmetries are broken. We consider

three types of superlattice: single layer, bilayer with $ABAB$ stacking, and bilayer with $ABCD$ stacking. A brief summary of our results is listed below.

For the single-layer Ir oxide, the Dirac dispersion at X and Y TRIM points is protected by the b -glide symmetry. When this b -glide symmetry is broken, for instance, by an uniaxial pressure, it reveals a 2D topological insulator by gapping the Dirac nodes. In the presence of a magnetic ordering or external magnetic field, the system becomes a topological magnetic insulator with QAH effects.

In the bilayer Ir oxides, we consider two different types of stacking. (1) For $ABAB$ stacking, the system is a semimetal with two nodal points at ϵ_F . Any finite magnetic field for any direction except the $[1\bar{1}0]$ axis or magnetic ordering turns the system into a topological magnetic insulator with QAH effects. Thus, the topological magnetic insulator in $ABAB$ stacking is more realizable in the current experiment setting than the single-layer case. (2) In the $ABCD$ stacking case, due to an additional mirror symmetry Π_{mirror} , it provides a richer phase diagram. Besides the QAH phase, there are two additional phases: TCI with nontrivial mirror Chern number and MVH insulators with quantized mirror valley Chern number.

Experimentally, these superlattices or films are grown along the $[001]$ axis, which can be achieved by a very standard PLD growing technique. To test the proposal, an ARPES measurement can be employed to investigate the Dirac points in these superlattices when TR symmetry is preserved, and a Hall conductivity measurement should exhibit the QAH effect when a magnetic ordering occurs or an external magnetic field is applied.

ACKNOWLEDGMENT

This work was supported by the NSERC of Canada and the Center for Quantum Materials at the University of Toronto.

APPENDIX: ANALYTICAL RESULTS OF $ABCD$ BILAYER

Applying the following canonical transformation in σ and ν space:

$$\sigma_{\pm} \rightarrow \sigma_{\pm} \nu_z, \quad \nu_{\pm} \rightarrow \nu_{\pm} \sigma_z, \quad (\text{A1})$$

the Hamiltonian in Eq. (15) can be brought into a block diagonalized form,

$$H' = \begin{pmatrix} H'_+ & 0 \\ 0 & H'_- \end{pmatrix}, \quad (\text{A2})$$

with

$$H'_{\pm} = \pm \epsilon_{di}(\mathbf{k}) \sigma_z + \epsilon_0(\mathbf{k}) \tau_x + \epsilon_y(\mathbf{k}) \sigma_y \tau_y + \epsilon_x(\mathbf{k}) \sigma_x \tau_y \pm t'_z (\sigma_x - \sigma_y) \tau_z, \quad (\text{A3})$$

where \pm subscripts are assigned to reflect the eigenvalues of $\sigma_z \nu_x$ and the basis we choose for H' is a set of the eigenvectors of $\sigma_z \nu_x$.

Let us consider the upper block Hamiltonian H'_+ near the X point for now. By computing the eigenvalues of H'_+ in Eq. (A3) along $X \rightarrow \Gamma$, the location where the band gap vanishes near

X is given by

$$\cos(k_0^\pm) = \pm \frac{t'_z}{t_1 - t_2}. \quad (\text{A4})$$

The two solutions $(k_0^\pm, -k_0^\pm)$ in Eq. (A4), in fact, have the same topological properties. For convenience, only one point $(k_0^+, -k_0^+) \equiv (k_0, -k_0)$ will be taken into account.

An effective two-band Hamiltonian can be obtained by projecting the H'_+ to the relevant two bands $|\phi\rangle$ and $|\varphi\rangle$ at $(k_0, -k_0)$,

$$\begin{aligned} |\phi\rangle &= \frac{1}{\sqrt{2}}(-|1, \downarrow\rangle + |2, \downarrow\rangle), \\ |\varphi\rangle &= \frac{1}{\sqrt{2}}(|1, \uparrow\rangle + |2, \uparrow\rangle), \end{aligned} \quad (\text{A5})$$

where 1 (2) refers to top (bottom) layer and $\uparrow(\downarrow)$ for $|J_z = \frac{1}{2}(-\frac{1}{2})\rangle$. Follow the perturbation theory, the effective two-band Hamiltonian around X is written as

$$H_{+,X}^{\text{eff}} = \hat{P}_0 H'_+ \hat{P}_0 = \vec{A}_{+,X}(\mathbf{k}) \cdot \vec{\sigma}, \quad (\text{A6})$$

where the projecting operator is $\hat{P}_0 = |\phi\rangle\langle\phi| + |\varphi\rangle\langle\varphi|$ and each component of $\vec{A}_{+,X}$ is given by

$$\begin{aligned} A_{+,X}^z &= t_z + t_{(110)} + t'_{(1\bar{1}0)} + t'_0 \equiv \delta_X, \\ A_{+,X}^{y/x}(\mathbf{k}) &= t'_1 \delta k_{y/x} - t'_2 \delta k_{x/y}. \end{aligned} \quad (\text{A7})$$

Here, $t'_1 = t_1 \sin(k_0)$, $t'_2 = t_2 \sin(k_0)$, $t'_{(1\bar{1}0)} = t_{(1\bar{1}0)} \sin(k_0)$, $t'_0 = 4t_0 \cos(k_0)$, and $\delta k_x \equiv k_x - k_0$, $\delta k_y \equiv k_y + k_0$ for the following calculation. The Berry curvature for the p th band is given as $\Omega_p(\mathbf{k}) = \nabla_{\mathbf{k}} \times (i \langle p, \mathbf{k} | \nabla_{\mathbf{k}} | p, \mathbf{k} \rangle)$. Thus the Berry curvature for the lowest band of $H_{+,X}^{\text{eff}}$ in Eq. (A6) is

$$\Omega_{+,X}^z(\mathbf{k}) = \frac{[(t'_2)^2 - (t'_1)^2] \delta_X}{|\vec{A}_{+,X}|^3}. \quad (\text{A8})$$

The Chern number can be computed using the formula of Eq. (7) given in the main text and the expression is quite straightforward,

$$C_{+,X} = \text{sign}(\delta_X). \quad (\text{A9})$$

Following the same procedure for lower block H'_- around X and \pm block around Y , the Chern number is given by

$$\begin{aligned} C_{\pm,X} &= \pm \text{sign}(\delta_X), \\ C_{\pm,Y} &= \mp \text{sign}(\delta_Y), \end{aligned} \quad (\text{A10})$$

where $\delta_Y = t_z + t'_{(110)} + t_{(1\bar{1}0)} + t'_0$ with $t'_{(110)} = t_{(110)} \sin(k_0)$.

Various topological charges in the bilayer system has been identified in Eq. (20). By plugging in the expression of Eq. (A10), we have

$$\begin{aligned} C_{mv} &= \text{sign}(\delta_X) + \text{sign}(\delta_Y), \\ C_m &= \text{sign}(\delta_X) - \text{sign}(\delta_Y), \\ C_v &= C = 0. \end{aligned} \quad (\text{A11})$$

Here, by considering the magnetic field along the z direction $h_z \sigma_z$ with $h_z > 0$, the TR can be explicitly broken. The only modification in the two-band effective Hamiltonian is that the mass term appears in Eq. (A8), which changes to

$$\delta_{X/Y} \rightarrow h_z \pm \delta_{X/Y}. \quad (\text{A12})$$

And the Chern numbers in Eq. (A10) have the following expressions:

$$\begin{aligned} C_{\pm,X} &= \text{sign}(h_z \pm \delta_X), \\ C_{\pm,Y} &= -\text{sign}(h_z \pm \delta_Y). \end{aligned} \quad (\text{A13})$$

The explicit expression of C_{mv} , C_m , C_v , and C in Eq. (20) can be modified accordingly based on Eq. (A13). The above analysis indicates that the phase transition is driven by the z -direction magnetic field h_z .

-
- [1] C. L. Kane and E. J. Mele, *Phys. Rev. Lett.* **95**, 146802 (2005).
 [2] B. A. Bernevig and S.-C. Zhang, *Phys. Rev. Lett.* **96**, 106802 (2006).
 [3] D. N. Sheng, Z. Y. Weng, L. Sheng, and F. D. M. Haldane, *Phys. Rev. Lett.* **97**, 036808 (2006).
 [4] B. A. Bernevig, L. H. Taylor, and S.-C. Zhang, *Science* **314**, 1757 (2006).
 [5] R. Roy, *Phys. Rev. B* **79**, 195322 (2009).
 [6] L. Fu and C. L. Kane, *Phys. Rev. B* **76**, 045302 (2007).
 [7] L. Fu, C. L. Kane, and E. J. Mele, *Phys. Rev. Lett.* **98**, 106803 (2007).
 [8] J. E. Moore and L. Balents, *Phys. Rev. B* **75**, 121306(R) (2007).
 [9] C. L. Kane and J. E. Moore, *Phys. World* **24**, 32 (2011).
 [10] M. König, S. Wiedmann, C. Bruce, A. Roth, H. Buhmann, L. Molenkamp, X. L. Qi, and S. C. Zhang, *Science* **318**, 766 (2007).
 [11] D. Hsieh, D. Qian, L. Wray, Y. Xia, Y. S. Hor, R. J. Cava, and M. Z. Hasan, *Nature (London)* **452**, 970 (2008).
 [12] D. Hsieh *et al.*, *Science* **323**, 919 (2009).
 [13] Y. Xia, D. Qian, D. Hsieh, L. Wray, A. Pal, H. Lin, A. Bansil, D. Grauer, Y. S. Hor, R. J. Cava, and M. Z. Hasan, *Nat. Phys.* **5**, 398 (2009).
 [14] Y. S. Hor, A. Richardella, P. Roushan, Y. Xia, J. G. Checkelsky, A. Yazdani, M. Z. Hasan, N. P. Ong, and R. J. Cava, *Phys. Rev. B* **79**, 195208 (2009).
 [15] D. Hsieh, Y. Xia, D. Qian, L. Wray, F. Meier, J. H. Dil, J. Osterwalder, L. Patthey, A. V. Fedorov, H. Lin, A. Bansil, D. Grauer, Y. S. Hor, R. J. Cava, and M. Z. Hasan, *Phys. Rev. Lett.* **103**, 146401 (2009).
 [16] M. Z. Hasan and C. L. Kane, *Rev. Mod. Phys.* **82**, 3045 (2010).
 [17] X. L. Qi and S. C. Zhang, *Rev. Mod. Phys.* **83**, 1057 (2011).
 [18] Liang Fu, *Phys. Rev. Lett.* **106**, 106802 (2011).
 [19] T. H. Hsieh, H. Lin, J. Liu, W. Duan, A. Bansil, and L. Fu, *Nat. Commun.* **3**, 982 (2012).
 [20] P. Dziawa *et al.*, *Nat. Mater.* **11**, 1023 (2012).
 [21] S.-Y. Xu *et al.*, *Nat. Commun.* **3**, 1192 (2012).
 [22] Y. Tanaka, Z. Ren, T. Sato, K. Nakayama, S. Souma, T. Takahashi, K. Segawa, and Y. Ando, *Nat. Phys.* **8**, 800 (2012).
 [23] G. E. Volovik, *Lect. Notes Phys.* **718**, 31 (2007).
 [24] S. Murakami, *New J. Phys.* **9**, 356 (2007).
 [25] A. A. Burkov, and Leon Balents, *Phys. Rev. Lett.* **107**, 127205 (2011).

- [26] X. Wan, A. M. Turner, A. Vishwanath, and S. Y. Savrasov, *Phys. Rev. B* **83**, 205101 (2011).
- [27] K. Y. Yang, Y. M. Lu, and Ying Ran, *Phys. Rev. B* **84**, 075129 (2011).
- [28] C. X. Liu, X. L. Qi, X. Dai, Z. Fang, and S. C. Zhang, *Phys. Rev. Lett.* **101**, 146802 (2008).
- [29] R. Yu, W. Zhang, H. J. Zhang, S. C. Zhang, X. Dai, and Z. Fang, *Science* **329**, 61 (2010).
- [30] G. Xu, H. Weng, Z. Wang, X. Dai, and Z. Fang, *Phys. Rev. Lett.* **107**, 186806 (2011).
- [31] C. Z. Chang *et al.*, *Science* **340**, 167 (2013).
- [32] S. A. Parameswaran, R. Roy, and S. L. Sondhi, *C. R. Phys.* **14**, 816 (2013).
- [33] W. Witczak-Krempa, G. Chen, Y. B. Kim, and Leon Balents, *Annu. Rev. Condens. Matter Phys.* **5**, 57 (2014).
- [34] J. M. Carter, V. V. Shankar, M. A. Zeb, and H. Y. Kee, *Phys. Rev. B* **85**, 115105 (2012).
- [35] J. Matsuno, K. Ihara, S. Yamamura, H. Wadati, K. Ishii, V. V. Shankar, H. Y. Kee, and H. Takagi, [arXiv:1401.1066](https://arxiv.org/abs/1401.1066).
- [36] D. Xiao, W. Zhu, Y. Ran, N. Nagaosa, and S. Okamoto, *Nat. Commun.* **2**, 596 (2011).
- [37] C. L. Kane and E. J. Mele, *Phys. Rev. Lett.* **95**, 226801 (2005).
- [38] H. Jin, H. Jeong, T. Ozaki, and J. Yu, *Phys. Rev. B* **80**, 075112 (2009).
- [39] R. Arita, J. Kunes, A. V. Kozhevnikov, A. G. Eguiluz, and M. Imada, *Phys. Rev. Lett.* **108**, 086403 (2012).
- [40] The spin quantization axis was chosen to match the local z axis of oxygen octahedron.
- [41] J. C. Slater and G. F. Koster, *Phys. Rev.* **94**, 1498 (1954).
- [42] S. J. Moon, H. Jin, K. W. Kim, W. S. Choi, Y. S. Lee, J. Yu, G. Cao, A. Sumi, H. Funakubo, C. Bernhard, and T. W. Noh, *Phys. Rev. Lett.* **101**, 226402 (2008).
- [43] B. J. Kim, H. Ohsumi, T. Komesu, S. Sakai, T. Morita, H. Takagi, and T. Arima, *Science* **323**, 1329 (2009).
- [44] I. Dzyaloshinskii, *J. Phys. Chem. Solids* **4**, 241 (1958); T. Moriya, *Phys. Rev.* **120**, 91 (1960).
- [45] J. M. Carter, V. Shankar, and H. Y. Kee, *Phys. Rev. B* **88**, 035111 (2013).
- [46] Y. Hatsugai, *Phys. Rev. Lett.* **71**, 3697 (1993).
- [47] The nodal points shown in Fig. 5(a) are connected and form a close degenerate line with dispersion $\cos(k_x) + \cos(k_y) = \frac{2t_z}{\sqrt{(2t_0-t_{12})^2+(t_{1d})^2} + \sqrt{(2t_0+t_{12})^2+(t_{1d})^2}}$; tight-binding parameters in the dispersion are given in the main text.
- [48] M. Ezawa, *Phys. Lett. A* **378**, 1180 (2014).
- [49] A very small amount of tilting degree may lead to electron and hole pockets of the Fermi surface. But it does not change the topological nature of the system qualitatively.
- [50] F. Zhang, J. Jung, G. A. Fiete, Q. Niu, and A. H. MacDonald, *Phys. Rev. Lett.* **106**, 156801 (2011).
- [51] K. F. Mak, K. L. McGill, J. Park, P. L. McEuen, *Science* **344**, 1489 (2014).